PHYSICAL REVIEW RESEARCH **7**, 033043 (2025)

Femtosecond laser-induced optical breakdown and cavitation dynamics in water imaged with an x-ray free-electron laser

Hannes P. Hoeppe,[1] Juan M. Rosselló,[2,3] Malte Vassholz,[1] Johannes Hagemann,[4] Markus Osterhoff,[1]
Thea Engler,[1] Angel Rodriguez-Fernandez,[5] Ulrike Boesenberg,[5] Johannes Möller,[5] Roman Shayduk,[5] Jörg Hallmann,[5]
Anders Madsen,[5] Robert Mettin,[5] and Tim Salditt[1,*]

[1]*Institut für Röntgenphysik, Georg-August-Universität Göttingen, D-37077 Göttingen, Germany*
[2]*Faculty of Mechanical Engineering, University of Ljubljana, SVN-1000 Ljubljana, Slovenia*
[3]*Physikalisches Institut, Georg-August-Universität Göttingen, D-37077 Göttingen, Germany*
[4]*CXNS - Center for X-ray and Nano Science, Deutsches Elektronen-Synchrotron DESY, D-22607 Hamburg, Germany*
[5]*European X-ray Free-Electron Laser Facility, D-22869 Schenefeld, Germany*

(Received 22 October 2024; accepted 1 May 2025; published 10 July 2025)

We investigate the ultrafast dynamics of plasma formation by optical breakdown, filamentation, and cavitation in water, using high spatiotemporal resolution offered by x-ray free-electron laser (XFEL) radiation. A femtosecond infrared laser pulse is focused in a water-filled cuvette and probed by a single femtosecond x-ray pulse, with a time delay covering nearly four orders of magnitude. By exploiting the quantitative contrast values obtained by phase retrieval, we can follow the transition from plasma to gas in terms of a continuous decrease of mass density in the cavity. At the same time, we image the emission of a cylindrical shock wave for the scenario of a single elongated breakdown filament with a high degree of symmetry. Contrarily, the regime of multiple breakdown spots deviates from cylindrical symmetry and the idealized picture expected for a Gaussian beam. Here different scenarios of cavitation and (collective) expansion dynamics as well as bubble fusion are observed. Specifically, we quantify the decrease of the expansion velocity with the number of auxiliary cavitation events due to a redistribution of the deposited laser energy. We also report events with (multi)filamentation reflecting instabilities in the initial distribution of the laser intensity upon formation of the plasma. Filaments with submicron diameter and few-micrometer spacing are observed, as well as the phenomena of filament emergence, splitting, and termination. The different regimes of heterogeneous optical breakdown and cavitation can be distinguished depending on the laser pulse energy. Altogether, the experiments demonstrate the potential of single-pulse XFEL imaging for the investigation of optical breakdown and ultrafast hydrodynamics. The future application of the imaging approach to soft matter environments, tissue, glasses, and opaque materials seems straightforward.

DOI: 10.1103/c91c-zrm7

I. INTRODUCTION

Femtosecond laser-induced optical breakdown in liquids and the subsequent formation of cavitation bubbles involves a complex interplay of nonlinear phenomena, which are highly relevant both for fundamental science and technology. In fact, it is the ultrafast processes and nonlinear effects of beam propagation which determine the cavitation dynamics, even on macroscopic length and timescales after impact. The basic phenomena associated with optical breakdown and cavitation can be summarized as follows: At ultrashort timescales, the process in transparent condensed media is dominated by multiphoton and tunneling ionization, leading to a spatially elongated deposition of energy and the formation of a plasma channel [1–5]. In the superthreshold regime of optical breakdown, the high-pressure plasma rapidly expands after thermalization, leading to the emission of a shock wave [6–11]. The plasma constituents recombine upon cooling, forming an elongated cavitation bubble consisting of gas and vapor. The bubble expands to a maximum radius and finally undergoes an inertial collapse, which can involve the formation of jets and bubble fragmentation, leaving a dispersed cloud of remnant bubbles behind [7,12–15]. The disruptive effects of femtosecond (fs) optical breakdown and cavitation, particularly in aqueous media and tissues, are exploited for important medical interventions, including ophthalmic surgery and tumor resection [5,16–19]. These applications take advantage of the precise spatial control of the laser pulse impact with minimized collateral damage.

At sufficient laser power, the balance of Kerr self-focusing and plasma defocusing leads to the formation of a continuous filament of excited matter [20–25]. Filamentation enables focused beam propagation over long distances, overcoming diffraction-induced beam divergence. Depending on the

---

[*] Contact author: tsaldit@gwdg.de

focusing geometry and intensity, filamentation in liquids leads to the formation of an elongated, quasicylindrical bubble or multiple hot spots along the optical axis, giving rise to a series of separated cavitation bubbles [13,15,26–28]. In solids, filamentation is exploited for laser bulk nanofabrication [29–34]. At the same time, filamentation involves a significant spectral broadening of the ultrashort pulse, i.e., supercontinuum generation, with potential use as a white-light laser source [22,35–39]. Further applications are found, for example, in atmospheric sensing [40], laser-induced breakdown spectroscopy [41], or water splitting [42,43].

Modulational instability or aberrations of the laser beam can lead to multifilamentation transversely to the optical axis [13,22,44,45]. Microfilaments can emerge, fuse, and interact with the surrounding low-energy plasma region [22,23]. Considering further nonlinear propagation effects like group-velocity dispersion, self-steepening, or pulse splitting, the intensity distribution of a focused fs laser pulse becomes a complex spatiotemporal problem.

While in collimated beams, filamentation structures are conveniently imaged and manipulated by optical techniques [46–48], details of microfilamentation in focused beams can be on the scale of the optical resolution limit and have rarely been resolved experimentally [49–51]. In solids, electron microscopy inspection was performed after laser ablation [52], which is not possible in soft matter or liquids, and also not easily extended to ultrafast timescales.

The recent advent of ultrafast imaging with single x-ray free-electron laser (XFEL) pulses now offers high spatial and temporal resolution, enabling the investigation of fast phenomena like shock-wave propagation in solids [53,54] or shock and cavitation dynamics in liquids [55–61]. To this end, inline holographic full-field imaging with phase contrast based on self-interference of the beam [62] is particularly advantageous since no scanning is required. The imaging scheme is based on phase retrieval algorithms and coherent beams, which allow the quantitative reconstruction of the electron density of the sample. While it is already well established for high spatial resolution in material and biomedical research, essentially, ultrafast imaging with XFEL pulses now extends this coherent x-ray imaging approach to high temporal resolution. For studies of optical breakdown and cavitation, it can capitalize on the advantages of high penetration capability and the fact that volumetric information is probed with almost no disturbance by curved phase boundaries or plasma. These disturbances are the major limiting factors in conventional optical imaging approaches, in addition to the Abbe diffraction limit for the spatial resolution.

In this work, we investigate the early dynamics of optical breakdown and cavitation bubble growth by single-pulse x-ray holography. We build on previous experiments investigating cavitation in water [63–65]. These experiments demonstrated the potential of time-resolved x-ray imaging with single FEL pulses to quantitatively investigate processes like shock-wave propagation and bubble growth. We now measure the dynamics in a time interval of over three orders of magnitude, from a few 100 ps to 1.2 μs, in a pump-probe scheme. The experiment was carried out at the materials imaging and dynamics (MID) instrument of the European XFEL Facility in Schenefeld, Germany [66]. High-resolution images reveal details of the dynamics of single or heterogeneous bubble growth from multiple breakdown hot spots, which were not yet observed experimentally. During the expansion of closely neighboring cavities, thin water layers separate the bubbles until they merge after about 1 μs after seeding. For events featuring a quasicylindrical symmetry, shock-wave emission, and bubble growth were observed and modeled in one-dimensional radial coordinates. In addition, the breakdown statistics and cavitation dynamics are investigated at different pump laser energies from 5 μJ to 124 μJ, corresponding to a peak intensity range of $3 \times 10^{14}\,\mathrm{W/cm^2}$ to $7.3 \times 10^{15}\,\mathrm{W/cm^2}$. In the low-energy regime, multifilamentation is observed to create separate filament-like cavities with diameters below 1 μm.

II. EXPERIMENTAL METHODS

The dynamics of fs optical breakdown and cavitation bubbles in water was investigated by full-field x-ray holography with single free-electron laser pulses, in a stroboscopic pump-probe scheme at 10 Hz repetition rate. The experiment was carried out at the Materials, Imaging, and Dynamics (MID) instrument of the European X-ray Free-Electron Laser [66]. An overview of the experimental setup is shown in Fig. 1.

Optical breakdown and cavitation bubbles in water were induced by ultrashort optical laser pulses from a Ti:sapphire laser system with a wavelength $\lambda_l = 800\,\mathrm{nm}$, available at MID. A pulse energy range from 5.4(3) μJ to 123(3) μJ was investigated, where the latter corresponds to a peak power density of approximately $7.3 \times 10^{15}\,\mathrm{W/cm^2}$, assuming a Gaussian profile with a beam waist of 9 μm and a pulse length of 50 fs. Note that it is possible that the pulse was slightly stretched due to dispersion effects accumulated on the custom beam path up to the sample position. The laser beam was focused by a 90° off-axis parabolic mirror with an effective focal length of $f = 75\,\mathrm{mm}$ ($\mathrm{NA} \approx 0.26$) into the experimental chamber, filled with deionized, filtered water (milli-Q). Alignment of the focusing mirror was optimized in air, by maximizing the air-plasma intensity. To allow positional alignment with respect to the fixed x-ray beam direction (x), both the water chamber as well as the pump laser beam path were designed with independent degrees of freedom, in the (x,y,z) and (y,z) directions, respectively.

The laser-induced cavitation process was imaged both by single-pulse x-ray holography as well as by optical high-speed imaging, from an observation angle orthogonal to the optical axis of the pump laser. The x-ray pulses were provided by the SASE2 undulator of the European XFEL, with a photon energy of $E_{\mathrm{ph}} = 18\,\mathrm{keV}$ and a mean pulse energy of 960 ± 160 μJ. This photon energy was mainly chosen to enable measurements in bulk water with long optical path lengths in the subsequent experiment [61]. No monochromator was used to maximize the flux. The beam was focused by a set of 50 nanofocusing Beryllium compound refractive lenses (CRLs), together with a corrective phase plate [67,68], creating a cone beam with 0.3 mrad half-divergence angle. The cavitation events were probed at a distance of $x_{01} = 102.4\,\mathrm{mm}$ behind the focus, and the x-ray holograms were recorded by a sCMOS camera, fiber-coupled to a LuAg scintillator

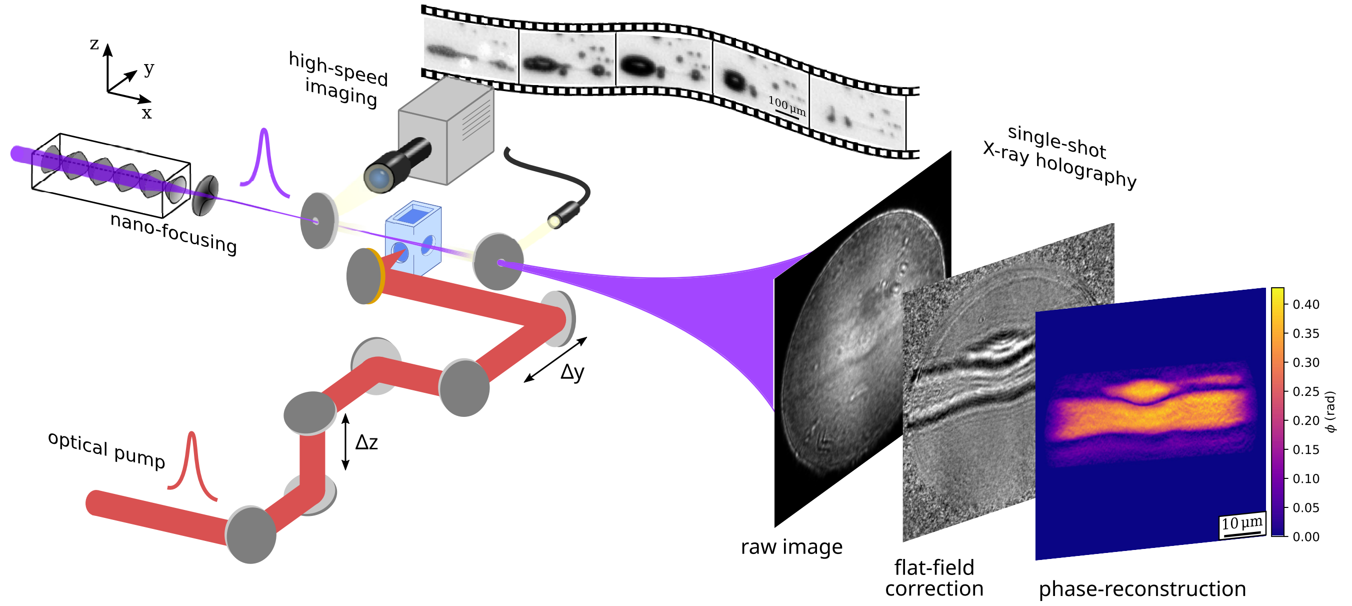

FIG. 1. Experimental setup and pump-probe scheme. A fs near-infrared pump laser is focused into a water-filled cuvette and generates an elongated optical breakdown plasma, which subsequently expands as a cavitation bubble. The process is probed by a single XFEL pulse after a variable delay Δt. The x-ray beam is focused by nano-CRLs to create a divergent beam geometry, with the sample at a distance $x_{01} = 102$ mm and the x-ray detector at $x_{02} = 9.867$ m behind the focus. The projected phase-image of the sample can later be reconstructed numerically from the x-ray holograms. The pump-probe experiment is conducted at 10 Hz repetition rate. Each event is additionally captured by optical high-speed imaging in the same direction of observation, with a frame rate of 1.2 MHz and in a back-light configuration.

(Zyla 5.5, Andor, UK) at a distance $x_{02} = 9876$ mm. After this distance of free-space propagation, the sample-induced phase contrast was enhanced and forms holographic interference fringes [69]. At the same time, we exploited the geometric magnification of $M = x_{02}/x_{01} = 96$ leading to an effective pixel size of $px_{\mathrm{eff}} = 71$ nm, with a read-out area of almost 1 Mpx. Depending on the image features and pulse characteristics, we reported a spatial resolution between 170 nm and 800 nm (see Fig. S7 of the Supplemental Material [70]). The holographic regime was characterized by the effective Fresnel number $F = px_{\mathrm{eff}}^2 M/\lambda x_{12} = 7.1 \times 10^{-4}$. Note, that the sample chamber was placed in air, and a vacuum flight tube with a length of 8 m was placed between the sample and detector. For analysis, first, principal component analysis (PCA)-based flat-field correction was performed [63] followed by numerical phase reconstruction, carried out to retrieve the object's projected electron density, as indicated in Fig. 1.

Phase retrieval is a key part of holographic imaging and implies the reconstruction of both the amplitude A and phase ϕ of a complex wave field from the measured intensity. With propagation-based x-ray holography, we specifically reconstruct the x-ray wave field $\Psi = Ae^{i\phi}$ directly behind the object from the hologram measured at the detector. Generally, the distortion of the x-ray wavefront depends on the local refractive index of the sample material, written as $n = 1 - \delta + i\beta$, where δ induces the phase shift and β accounts for absorption. For water at the present x-ray energy $\beta/\delta = 7 \times 10^{-4}$, rendering the absorption almost negligible for the present phase-contrast imaging approach. The phase shift ϕ is inversely proportional to the projected electron density. If the sample consists of a homogeneous material, which can be assumed for pure vapor bubbles in water, ϕ is also strictly proportional to the projected mass density ρ, yielding

$$\phi = \phi_{\max}\left(\frac{\rho}{\rho_0} - 1\right), \tag{1}$$

where ρ_0 is the density of equilibrium water, $\phi_{\max} = k\delta d_{vx}$ is the phase shift introduced by the density difference between water and a vacuum in a volume element with length d_{vx}, and $k = 2\pi/\lambda$ is the x-ray wave number.

Depending on the degree of symmetry of the observed scene, phase-reconstruction was carried out in two dimensions with standard algorithms [71], or in one dimension radial coordinates using a model fit. A detailed description of the image processing and phase-reconstruction is given in the Supplemental Material [70].

A wide range of delays between the optical pump laser and the XFEL probe pulse was scanned, from the early picoseconds after laser incidence, up to over a microsecond where the bubble has expanded almost to its maximum (cylindrical) radius of approx. 35 µm. This was realized by the combination of three different delay mechanisms: (1) An optical delay line (DL800) was used to sample a time interval of 670 ps in steps of 1.67 ps. (2) An "RF delay" with an intermediate range was used to scan a time interval of 9 ns with steps of 45 ps. This delay mechanism is based on the radio frequency phase shift between the pump laser oscillator and the XFEL pulses, which is usually used only for synchronization. (3) An electronic trigger can be used to define delays in rough steps of 18 ns, corresponding to the XFEL accelerator's electron bunch buckets. In this experiment, a time interval of 1.2 µs was scanned with 160 ns steps. An overview of all measurements and delays with different combinations is shown in Fig. S1 in the Supplemental Material [70]. The temporal overlap between the XFEL pulse and the IR laser pulse was determined by a fast diode (rise time ≈200 ps), placed behind the sample-interaction region in the x-ray beam path. The diode detected both the x-ray pulse as well as the diffuse scattering of the pump laser from a paper target, placed at 45° at the sample position.

In parallel to the x-ray imaging, each cavitation event was recorded by optical high-speed shadowgraphy. Two drilled mirrors placed at a 45° angle, which passed the x-ray beam, allowed optical observation coaxially to the x-ray beam. Backlight 100 µs flash illumination (LED P40, Kistler, Switzerland) was employed, so that the collimated white light passed the water chamber and was captured by a high-speed camera (Fastcam SAZ 2100 K, Photron, Japan), equipped with a long-distance microscope. For each pump and probe pulse delivered with 10 Hz, a series of 50 frames was recorded with 1.2 MHz frame rate and a shutter speed of 160 ns, which captured the long-term evolution of bubble growth and collapse.

III. RESULTS AND DISCUSSION

The characteristics of optical breakdown can, in part, be described by the idealized picture of a Gaussian beam, subject to nonlinear optic phenomena and absorption. However, aberrations and modulational instability can lead to a nondeterministic complex intensity distribution in the focal volume. We recorded a variety of different cavitation scenarios including quasicylindrical symmetric events, distorted bubbles, or multiple separated bubbles. We begin by presenting the symmetric events which offer access to the radial density profile and then discuss the case of multibubble generation. In both cases, the laser pulse energy is kept constant at $E_p = 53$ µJ and the expansion dynamics is quantified. Second, we report the effect of varied laser pulse energy on the breakdown and cavitation characteristics. In particular, we discuss the observed multifilamentation within the focal volume of the laser pulse. The underlying image analysis of x-ray holograms, involving numerical phase reconstruction, and the determination of density is explained in the methods section and detailed in the Supplemental Material [70].

A. Bubble expansion dynamics from single breakdown filaments

First, the expansion dynamics of the cavitation events with quasicylindrical symmetry is discussed. An overview of the expansion dynamics is given in Fig. 2. In Fig. 2(a), the two-dimensional (2d) phase-reconstruction of selected single-pulse events is presented for increasing pump-probe delay Δt. The laser pulse is incident from the left, and the optical axis is slightly angled downward, by approximately 1.6°. Note that the x-ray field-of-view (FOV) is given by the CRL's numerical aperture (see Fig. 1) and the defocus distance. Here, the elongated cavities extend beyond the FOV to the left and right. The FOV is indicated by the red circle in the first frame of the optical images in Fig. 2(b). The images are additionally cropped vertically, according to the extent of the object.

For $\Delta t < 3$ ns the early cavity is visible as a thin filament, with weak total phase signal compared to noise and background fluctuation. Still, slight shape distortions in the form of kinks or nodes with increased thickness are visible. These are believed to be due to distortions and high-energy regions within the plasma filament. The oscillating behavior of thin sections and nodes corresponds to self-focusing and plasma-defocusing cycles on the length scale of 10 µm. This is a notably smaller length scale than the typical spacing between multiple breakdown events and refocusing cycles on the order of 100 µm which have been observed before [13], and which we also observe in the images of the optical camera.

After a few nanoseconds, a homogeneous filament then forms and for up to ≈200 ns the cavitation bubble expands radially in a quasicylindrical symmetry. At $\Delta t \geqslant 300$ ns the radial extent approaches the scale of the elongation, forming an elliptical cavitation bubble. The complete life cycle of the bubble expansion and collapse is captured by optical high-speed imaging. Figure 2(b) shows consecutive frames of a single event. The FOV of the multiple breakdown spots generate separate cavitation bubbles along the optical axis due to the refocusing within the laser filament. The main bubble reaches its maximum volume at approximately 2.6 µs and collapses along the optical axis, leaving a distribution of floating bubbles that slowly rise in the liquid.

In the first frame, remnant bubbles from the previous event are observed and can lead to scattered laser light, visible as bright spots in the shadow images. Note that the scatted light belongs to the blue-shifted part of the frequency-modulated spectrum, as it passes the short-pass frequency filter (750 nm) of the optical camera. During the passage of the shock or pressure wave emitted from the main event, the floating bubbles expand and collapse again, together with the main event.

Next, we turn to the analysis of the early transition from plasma to cavitation bubble, presented in Fig. 3. Since the signal-to-noise ratio for early delays is low, the x-ray holograms of these events are additionally processed with an alternative phase-reconstruction approach in one dimension, exploiting the cylindrical symmetry and signal accumulation of several pulses. To this end, the holograms are rotated by 1.6° and averaged horizontally. Further, the ensemble average over multiple single-pulse events within delay bins of 200 ps is computed. Figure 3(a) depicts the intensity map of the averaged profiles, lined up for different Δt. Within 10 ns, the central fringe corresponding to the cavity, develops increasing contrast. In addition, the shock wave gives rise to two holographic fringes which symmetrically diverge from the boundary of the cavity to the edge of the FOV. To analyze this data, a one-dimensional (1d) phase-reconstruction scheme is implemented in the form of a parameterized forward-propagation model. The predicted intensity profile in the detector plane can then be fitted to the fringes of the hologram to obtain the parameterized mass density distribution $\rho(r)$ of the cavitation region. More specifically, $\rho(r)$ is modeled as a series of step-functions, with the parameter r_b and r_s for the locations of the bubble boundary and shock front, a constant density ρ_b of water vapor inside the bubble and the pressure ρ_s at the shock front, respectively [see Fig. 3(c)]. Further details are given in the Supplemental Material [70]. In Fig. 3(b), 1d intensity profiles (solid) and the standard deviation (colored area) are depicted together with the model fit (black dashed) for selected Δt. Figures 3(d) and 3(e) show the radial trajectories and density values of the cavity and shock wave, respectively.

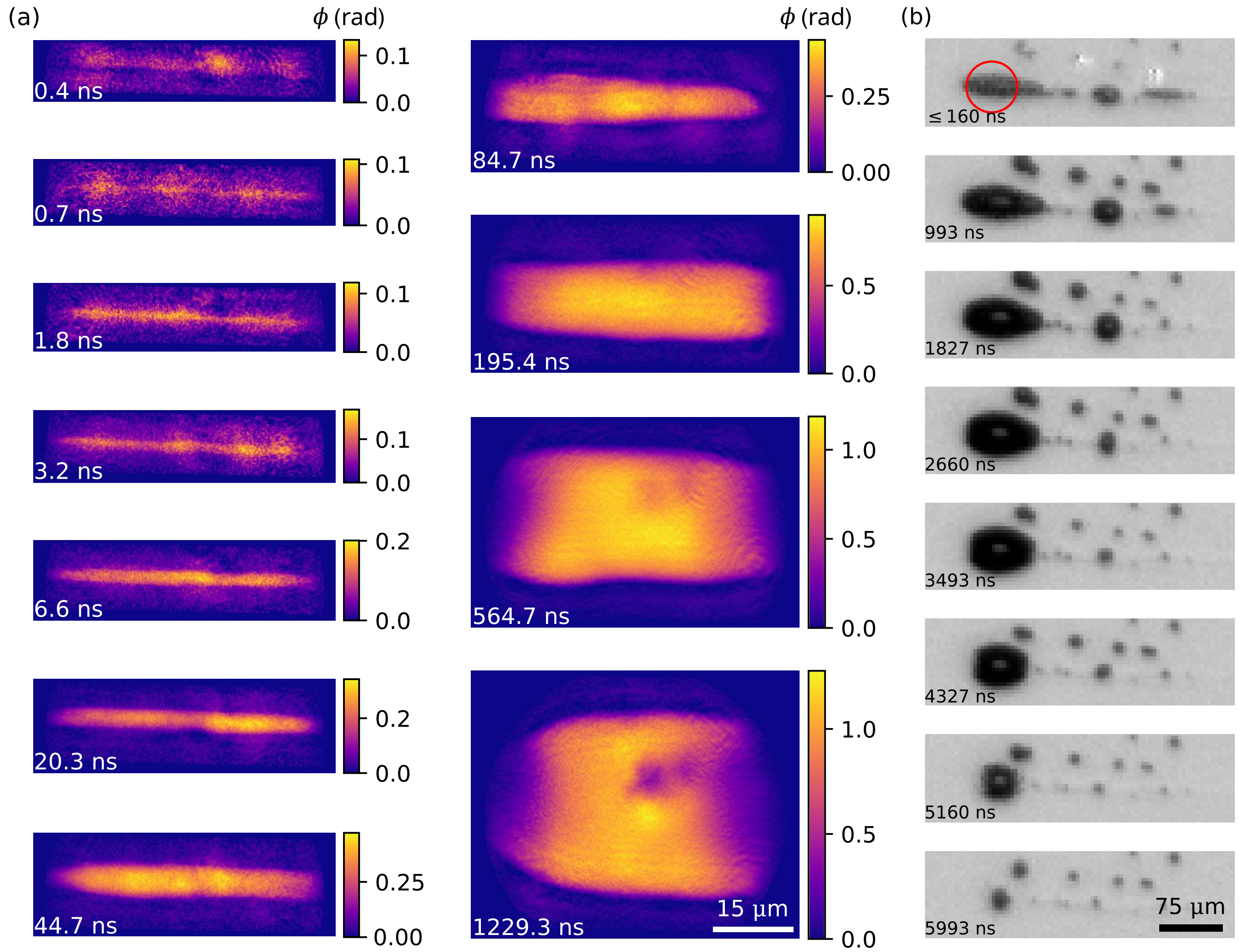

FIG. 2. Cylindrical symmetric bubble expansion. (a) Time series of selected x-ray phase-images of expanding bubbles exhibiting cylindrical symmetry. The vertical image size is adapted according to the expansion state of the cavity. The delay Δt is given in the bottom left corner of each image. (b) Optical high-speed imaging series of the bubble expansion and collapse. The consecutive frames correspond to the event depicted in (a) which is probed at 195 ns. The associated x-ray FOV is indicated by the red circle in the first frame.

The formation of the cavity starts at the initial size of the high-energy region of the breakdown plasma volume. Its expansion is comparably slow, but can be well described by a linear function in the observed time window, with the bubble wall velocity $v_b = 63(3)\,\mathrm{m/s}$ and initial radius $r_{b,0} = 0.91(2)\,\mu\mathrm{m}$. At the same time, the internal density decreases from $1\,\mathrm{g/cm^3}$ to $0.5\,\mathrm{g/cm^3}$ within 10 ns during the transition from the dense plasma to a gas and vapor-filled bubble [see Fig. 3(e)]. The independently recunstructed density values are consistent with a mass-conserving expansion (gray curve), considering the fitted linear expansion and the initial density $\rho_0 = 0.994\,\mathrm{g/cm^3}$. Note that the assumption of pure H_2O is justified for the phase reconstruction, even in the presence of other possible plasma-recombination products like H_2, O_2, or H_2O_2 [42] since the different species can be assumed to be homogeneously distributed and presumingly also of smaller concentration.

The shock wave propagates with a constant velocity of $v_s = 1574(9)$, m/s with an offset (y-intercept) of $r_{s,0} = 1.84(7)\,\mu\mathrm{m}$, as determined by a linear fit for $\Delta t > 4$ ns. The speed of the shock front v_s is close to the speed of sound in pure water. This linear regime is reached quickly, after a highest velocity of 1960(50), m/s is obsevered around 1.3 ns. This is in line with previous observations at comparable pulse energy, suggesting that the shock speed relaxes from its initial speed of potentially high Mach numbers to a velocity close to the speed of sound within only a few nanoseconds [8,72], followed by a propagation with a constant velocity [28,73,74].

At early delays of $\Delta t < 1.2$ ns, the shock wave cannot clearly be separated from the boundary of the cavity. The fit values for both R_b and R_s exhibit larger errors, yet they significantly deviate from the linear trend of the later dynamics. Such stationary or even converging dynamics of the initial cavity and shock front are unphysical and may be due to the limitations of the parameterized model and the low signal at the earliest delays. This inconsistency motivates comprehensive simulations [4] and improved imaging for the low-contrast regime, as discussed in [61]. However, as is exemplified in Fig. S4, the model fit including the shock wave is indeed necessary to fit the measured holograms, even for

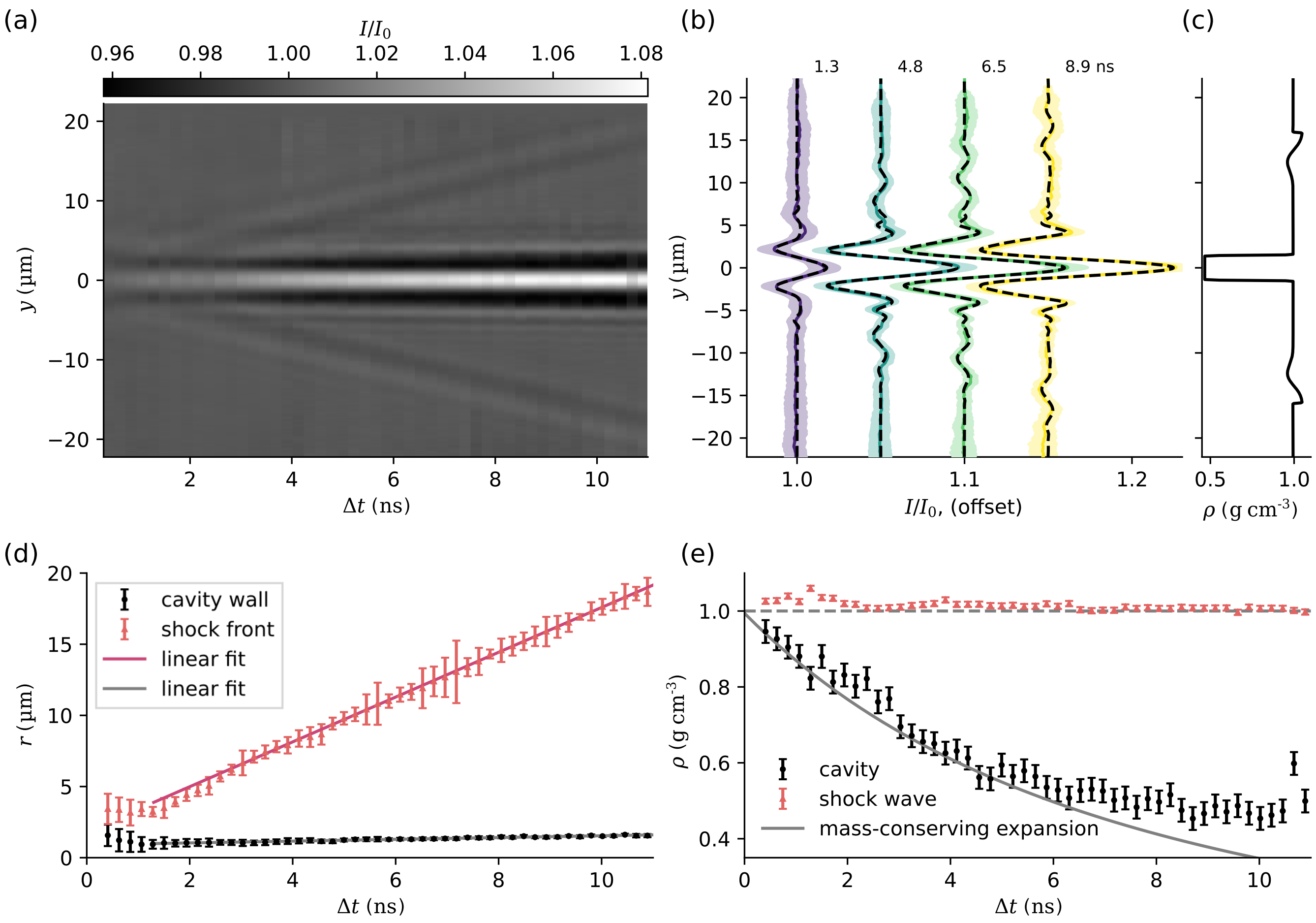

FIG. 3. Early bubble growth and shock wave emission. (a) Holographic intensity map of horizontally averaged images, which are lined up for different Δt. Each column represents the mean of all single-pulse profiles within a delay bin of 200 ps. (b) Average intensity profiles $I(y)$ of selected Δt (lines) and standard deviation (area). The forward-propagation model fit is plotted as the black dashed curve. (c) Model density profile $\rho(r)$ that is used to fit the 1d data, here illustrated for $\Delta t = 8.9$ ns. (d) Radial trajectories of the cavity wall (black) and shock front (red), obtained by the fits. A linear fit of the respective trajectories yields a shock velocity of 1574(9) m/s with a radial offset of 1.84(7) µm and a cavity expansion with 63(3) m/s and an initial radius of 0.91(2) µm. (e) Mass density of the vapour cavity interior (black) and the shock-compressed water (red), obtained by the fit. The gray curve corresponds to a mass-conserving expansion based on the linear fit determined in (d).

$\Delta t < 1.2$ ns. Here, we must conclude that a region of water in close proximity to the breakdown filament is gradually compressed during the initial cavity formation. The pressure wave is then only launched after the accumulation of sufficient mass at $\Delta t \approx 1$ ns. In contrast to the conclusion of [8,72], this mechanism does not involve an initially high Mach number.

The density values of the compressed water are close to unity for $\Delta t > 4$ ns, as expected for a weak shock or acoustic wave. Here we find a mean density of 1.010(7) g/cm^3, following the initial maximum of 1.060(7) g/cm^3 at 1.3 ns. The corresponding acoustic pressures are approximately 41(20) MPa in the weak shock regime and 192(25) MPa at the initial maximum, according to the modified Tait equation of state [75]. A direct link between the shock trajectory and the compression state of water would be very desirable. However, the equation of state, and correspondingly, the speed of sound depends on the water temperature as a free parameter. The water temperature could not be measured, but heating of several degrees can be estimated, based on the combined effects of the high-power LED illumination, x-ray absorption as well as the laser pulse itself. The measured shock trajectory and reconstructed compression values are indeed consistent when assuming a water temperature of $T = 37(6)\,^\circ$C. This can be calculated within the theory for weak shock waves [76] with the relation $p = 2\rho_0 c_0 (v_s - c_0)/\beta$ between the pressure p and the velocity v_s of the shock front and the Tait equation of state. Here, equilibrium density ρ_0, the speed of sound c_0, and the nonlinearity parameter β are temperature dependent [77]. The above-stated pressure values are calculated using this estimation.

For shock waves with Gigapascal pressures, it was already shown in previous work [65] that x-ray phase-contrast imaging provides a direct quantitative measurement of the compression state of water, independent of measurements of the propagation velocity of the shock front. We estimated the error for the reconstructed densities as the standard deviation of the ensemble data in the weak shock regime since the directly obtained fit errors were underestimated. In addition, the quantitative values of density or pressure reported here should be interpreted cautiously since they are very sensitive

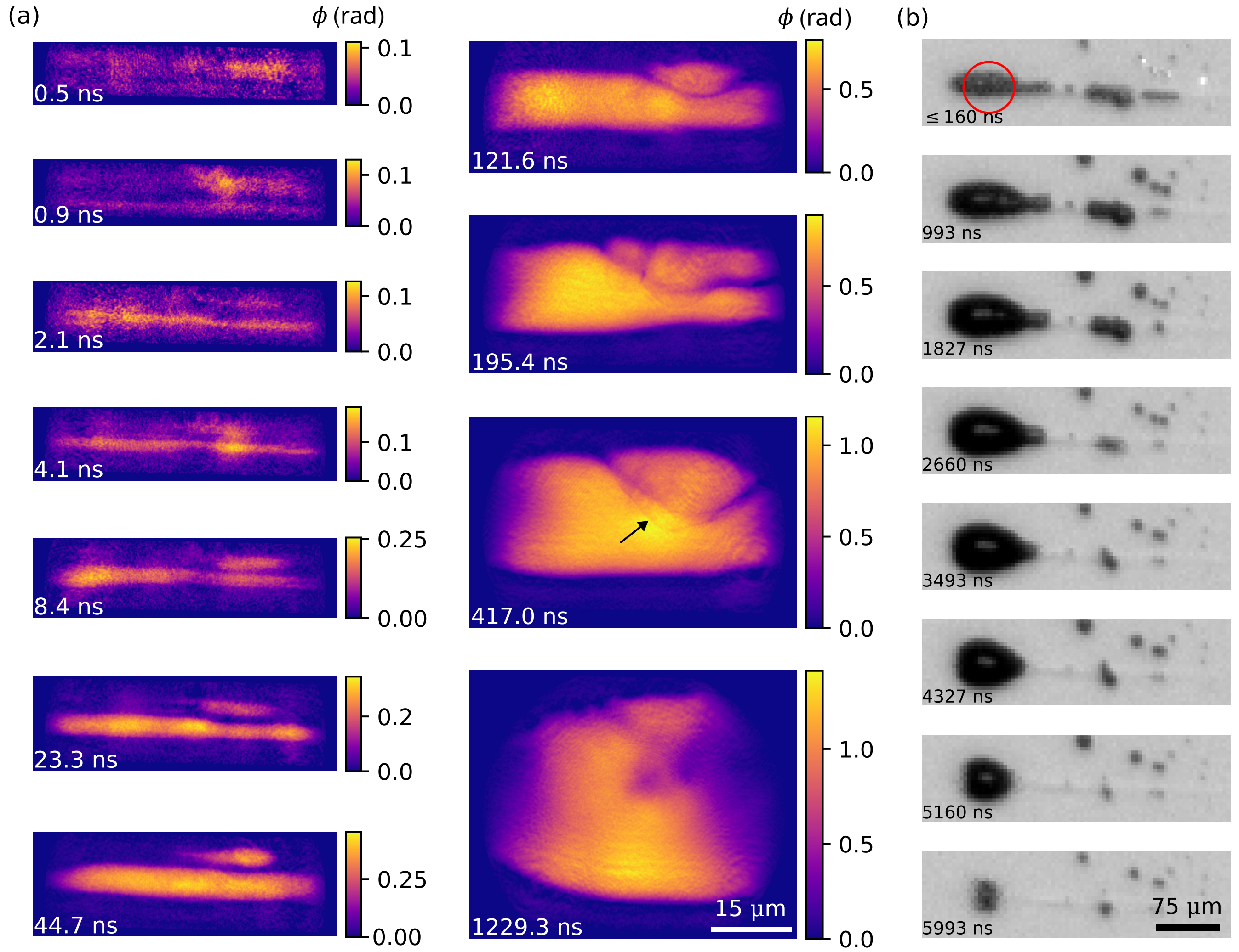

FIG. 4. Bubble expansion with a neighboring breakdown spot. (a) Time series of selected x-ray phase images of expanding bubbles that feature a second breakdown spot above the main filament. The image size is adapted according to the expansion state of the cavity. The delay Δt is given in the bottom left corner of each image. (b) Optical high-speed imaging series of the bubble expansion and collapse. The consecutive frames correspond to the event depicted in (a) that is probed at 195 ns. The x-ray FOV is indicated by the red circle in the first frame.

to systematic errors. For example, we expect ρ_s to be slightly underestimated compared to single events with a high degree of symmetry since ρ scales with the fringe contrast, which can be reduced by ensemble averaging of slightly deformed events. Later times of the bubble expansion dynamics are discussed further below, together with the collective dynamics of multiple bubbles.

B. Collective bubble expansion from multiple breakdown spots

The generation of multiple breakdown spots and the subsequent growth of adjacent cavitation bubbles can result from aberrations or random fluctuations like modulational instability which lead to multifilamentation. In Fig. 4, selected events are shown which feature a second, smaller cavity, located in the upper right corner relative to the main cavity. This scenario is frequently observed in two-cavity events, and should hence be attributed to aberrations. Similar to Fig. 2, the two left columns present 2d phase reconstruction at increasing Δt, as indicated in the image corner. Initially, the side cavity is vertically offset by approximately 4 µm from the main cavity. Both bubbles grow simultaneously, while the side cavity is slightly pushed outwards. As the bubbles grow into the gap between them, they remain separated by a thin layer of water, with a smallest resolved width of 600 nm, as is visible in Fig. 4(a), for $\Delta t = 121.6$ ns, 195.4 ns, and 417.0 ns. Parts of this water layer are interleaved by the volume of the main bubble (marked by the arrow), albeit still visible in the x-ray projection. At around 1 µs the water boundary has dissolved and the bubbles have joined.

Figure 4(b) shows an optical high-speed imaging sequence of a single event, corresponding to $\Delta t = 121.6$ ns of Fig. 4(a). At the given resolution of the optical recordings, the expansion and collapse dynamics of the bubble appears similar to the case of a single event [compare Fig. 2(b)]. Consequently, the micrometric cavitation scenario of small adjacent cavities does not critically influence the long-term bubble dynamics and related after effects. This is relevant for applications like

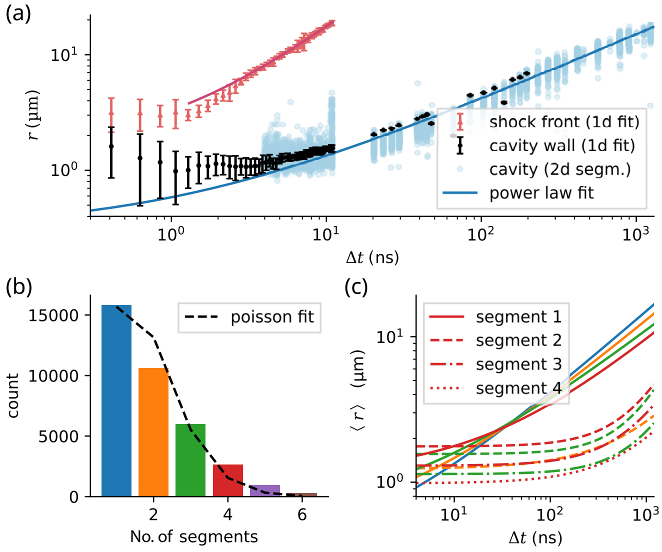

FIG. 5. Long timescale and collective cavity expansion dynamics. (a) Combined results from the analysis approaches of the 1d forward-propagation fit (early timescales) and the 2d phase reconstruction (later time scales). Blue scatter data represent the effective mean radius of the single-segment cavitation bubbles from the 2d phase reconstruction. The dynamics is fitted with a power-law function; the fit parameters are given in Table I. (b) Histogram of events with a certain number of separate breakdown events or cavitation bubbles, respectively. (c) Collective expansion dynamics of the cavitation bubbles. Colors indicate the events with a certain number of segments, similar as in (b). The power-law fit for $\langle r\rangle(\Delta t)$ is plotted for up to the fourth segment, with the nth segment indicated by the line style.

bubble-mediated tissue dissection or surface processing of materials in a liquid [17,78–80]. On the other hand, inference from the large-scale bubble dynamics on the breakdown scenario is not always possible down to the micrometric scale. This is an important limit for the typical assumption that the bubble shape encodes complete information about the breakdown scenario. Shock-wave emission, for example, is greatly influenced by the initial distribution of breakdown spots [81]. In contrast to the case of quasicylindrical symmetry, separate shock waves originating from a heterogeneous breakdown distribution do not interfere constructively, leading to significantly smaller peak pressures [27,72].

In the following, we show that the number of separate laser-induced cavities does influence the average size or the expansion dynamics, respectively. Two-dimensional phase reconstruction was carried out for all recorded images. Separate cavities were identified in each phase image, by a segmentation process that is based on image filtering, connected component analysis, and a watershed method (see Sec. 1 of the Supplemental Material [70]). Figure 5(a) shows the mean cavity radius for events with only one laser-induced bubble, obtained by segmentation of the single-pulse images (blue dots). For comparison, the results obtained by the 1d analysis are plotted again, on a logarithmic timescale (shock front: red, cavity wall: black). The 2d segmentation works well for $\Delta t >$ 10 ns, where images have a comfortable signal-to-noise ratio and cavities induce a total phase well above the background fluctuation. In this regime, a 2d analysis is especially valuable since the bubbles develop increasingly deformed shapes. As a result, $r(\Delta t)$ obtained from the 1d approach which assumes cylindrical symmetry constitutes an upper limit for the expansion dynamics.

TABLE I. Parameters of the power-law fit $r(\Delta t) = a\Delta t^b + r_0$ shown in Fig. 5(c), for the mean radius of separate cavitation bubbles, identified by segmentation of the 2d phase images. For a total number of n segments up to 4, the parameters are given for each nth segment.

nth segm.	a/kms^{-1}	b	r_0/µm
1	5.1(2)	0.577(3)	0.31(2)
1	5.7(6)	0.557(8)	0.50(6)
2	$7(6) \times 10^{-6}$	0.88(6)	1.24(3)
1	9(2)	0.52(2)	0.6(2)
2	$1(1) \times 10^{-5}$	1.4(1)	1.56(4)
3	$1(1) \times 10^{-5}$	1.4(2)	1.14(3)
1	0.003(2)	0.57(4)	1.1(2)
2	$2(5) \times 10^{-5}$	1.3(2)	1.76(7)
3	$9(15) \times 10^{-5}$	1.2(2)	1.30(5)
4	$1(2) \times 10^{-3}$	1.0(2)	0.98(4)

The expansion dynamics was measured up to 1.2 µs. In this time span, the growth of the bubble decelerates but does not reach its point of maximum expansion, i.e., inflection, at $\Delta t \approx$ 3 µs. As a consequence, the measured expansion dynamics could be fitted by a power law $r(\Delta t) = a\Delta t^b + r_0$, with the fit parameters given in Table I, but notably $b = 0.577(3)$. A description of the expansion with a suitable hydrodynamic bubble model, including the elliptical deformation, can be envisioned for future work. The histogram in Fig. 5(b) shows the distribution of recorded images that feature a certain number n segments, that is, cavitation hot spots. A fit of the shifted Poisson-like distribution $P_\mu(k-1)$ yielded $\mu = 0.84(8)$, albeit with a slight deviation in shape. For the subgroups featuring n cavitation bubbles as encoded by the color in the histogram, the mean radius $\langle r\rangle(t)$ of the n_{th} cavitation bubble is shown in Fig. 5(c). For each subgroup, only the power-law fit is depicted, with the fit parameters given in Table I. The presence of additional adjacent breakdown spots decelerates the expansion of the main cavitation bubble. In this case, the total deposited energy in the focal volume is redistributed to the neighboring plasma hot spots. This is also explained by the observation that the size of the nth auxiliary bubble increases with the number n of present cavitation hot spots.

C. Multifilamentation and pulse energy variation

Laser-induced breakdown and cavitation was investigated at varied pulse energies E_p in five steps between 123 and 5.4µJ, including the measurements at $E_p = 53$ µJ, which were discussed in the previous sections. With increasing E_p, the extent of the breakdown region both grows and shifts axially towards the source due to increased self-focusing of the beam. At different energies, we thus observe varying breakdown and filamentation scenarios within the fixed FOV, depending on the pulse propagation along the optical axis. These include the start of the breakdown region, initial filament splitting, and multiple separated micrometric filaments. Note that for

TABLE II. Overview of laser pulse parameters and thresholds. At given attenuator transmission T_{att}, the total pulse energy E_p was measured at the sample position for >500 single pulses, with the standard deviation indicated in the parentheses. The peak power is defined as $P_p = 0.94E_p/\tau$ and the peak intensity as $I_p = 2P_p/(\pi w_0^2)$, with a pulse width of $\tau_{\mathrm{fwhm}} \approx 50\,\mathrm{fs}$ and beam radius estimate of $w_0 \approx 4.5\,\mu\mathrm{m}$. For the lowest energy, a second estimate for $w_0 \approx 3.3\,\mu\mathrm{m}$ is given in an additional row (red), for the position at which multifilamentation is observed. The critical power for self focusing is $P_c = 1.5 \times 10^7$ W [20,82] and the breakdown threshold $I_{\mathrm{th}} \approx 1.3 \times 10^{13}\,\mathrm{W/cm^2}$ [4].

$T_{\mathrm{att}}/\%$	$E_p/\mu\mathrm{J}$	P_p/GW	P_p/P_c	$w_0/\mu\mathrm{m}$	$I_p/\mathrm{Wcm^{-2}}$	I_p/I_{th}
1.3	5.4(3)	0.1	7	4.5	3×10^{14}	25
1.3	5.4(3)	0.1	7	3.3	6×10^{14}	46
2.5	11.2(5)	0.21	14	4.5	7×10^{14}	51
5	24.0(7)	0.45	30	4.5	1.4×10^{15}	110
10	53(1.3)	0.99	65	4.5	3×10^{15}	240
20	123(2.5)	2.32	150	4.5	7.3×10^{15}	560

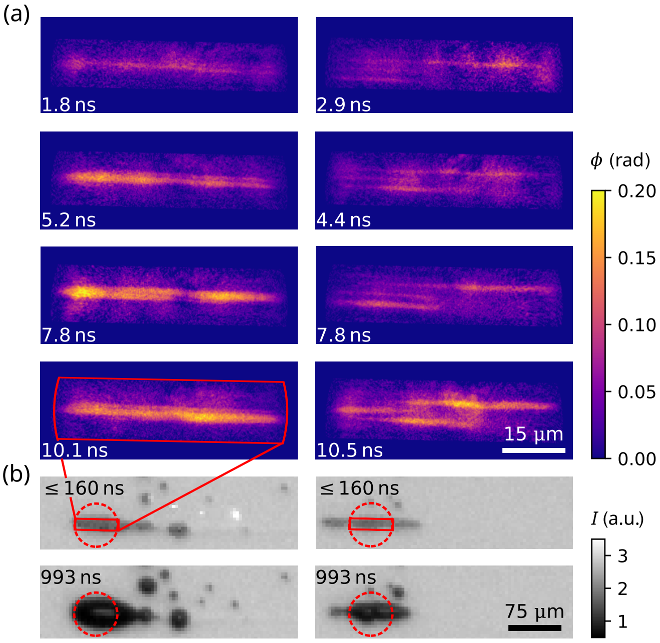

FIG. 6. Multifilamentation scenarios at different laser pulse energy and axial position. Comparison of breakdown regimes of laser pulse energy $E_p = 53\,\mu\mathrm{J}$ (left column) and $E_p = 5.4\,\mu\mathrm{J}$ (right column). The case of lower energy corresponds to a region located 50 μm downstream along the optical axis. (a) Time series of early bubble expansion for typical scenarios, which are observed at the given E_p. The pump-probe delay Δt is indicated in the bottom left corner of each image. (b) Two first frames of the optical high-speed imaging series of the event which is depicted in the last frame of each column in (a). The region of interest and the x-ray FOV are indicated by the red rectangle and circle, respectively.

early delays of a few nanoseconds, the laser-induced cavities reflect the deposited energy, i.e., the spatiotemporal intensity distribution of the laser pulse within the focal volume. Even for the lowest investigated pulse energies, the peak power exceeds the critical power for self-focusing given for a Gaussian pulse shape as [20,82]

$$P_c = 0.77\frac{\lambda_l^2}{4\pi n_0 n_2} = 1.55 \times 10^7\ \mathrm{W}. \tag{2}$$

Here, $\lambda_l = 800\,\mathrm{nm}$ is the wavelength of the pump laser and $n_0 = 1.33$ and $n_2 = 1.9 \times 10^{-16}\,\mathrm{cm^2/W}$ are the zeroth- and second-order refractive indices of water, respectively [83]. Similarly, for all measurements, the intensity in the focal area exceeds the threshold for the optical breakdown of $I_{\mathrm{th}} \approx 1.3 \times 10^{13}\,\mathrm{W/cm^2}$ as determined by Vogel *et al.* [4] (see Table II for an overview of the experimental parameters and thresholds).

In Fig. 6 typical scenarios observed at $E_p = 53\,\mu\mathrm{J}$ (left column) and $E_p = 5.4\,\mu\mathrm{J}$ (right column) are compared. Figure 6(a) shows a time series of the reconstructed x-ray phase-images, while in Fig. 6(b) the first two frames of the optical high-speed imaging series are shown. The x-ray FOV is highlighted in red. A complete overview of the scenarios observed for all investigated energies is depicted in Fig. S5, in the Supplemental Material [70]. At higher energy, a single quasicylindrical cavity is frequently observed and the FOV captures the region close to the beginning of the breakdown zone. Here, the onset of filament splitting can be observed as a substructure in some events but filaments have not yet separated. At $E_p = 5.4\,\mu\mathrm{J}$ we observe the central part of the breakdown region as the position of the geometric focus was moved towards the source by 50 μm. In this low-energy scenario, multiple separated filament-like cavities were observed. These are either aligned in parallel or show a slight divergence angle. In Fig. 6 (right column) a time series of events featuring three filaments is shown. Further examples of multifilamentation events are depicted in Fig. S6 in the Supplemental Material [70]. Remarkably, the initial diameter is as small as 700 nm, with a distance of approximately 1.2 μm between the nearest-neighboring cavities, and approximately 4.8 μm between the outermost filament-like cavities. This is on the same scale as predictions for the spacing of multiple filaments by Campillo *et al.* [84], describing multifilamentation as the growth of transverse wave components from modulational instability of a collimated beam in gas. With an estimation of the beam diameter of 6.6 μm and a peak intensity of $I_p = 5.9 \times 10^{14}\,\mathrm{W/cm^2}$, we obtain [22,84]

$$d_{\mathrm{fil}} = \sqrt{\pi P_c/I} = 2.8\,\mu\mathrm{m}. \tag{3}$$

This indicates that the multifilamentation events observed at $E_p = 5.4\,\mu\mathrm{J}$ in the center of the breakdown region have formed upon propagation and due to modulational instabilities of the laser pulse. This is in contrast to the multiple breakdown events at $E_p = 53\,\mu\mathrm{J}$ which were discussed above in Figs. 4 and 5, and where aberrations are suspected to be the dominant reason for multiple breakdown spots.

A comparison of the different relative positions along the optical axis which were measured at the different energies (see Fig. S5) allows us to infer the length scale of splitting of a single filament upon propagation. In the present intensity range and focusing geometry, filament splitting is first observed approximately 50 μm behind the breakdown region and fully developed after another 50 μm of propagation. Interestingly, this is in line with results obtained by Majus *et al.* [50] using an elliptically focused beam in fused silica. At the same time, the present high-resolution measurements for the case of a tightly focused beam stand out from measurements of multifilamentation at a larger spatial scale relevant for collimated and loosely focused beams, in which multiple filaments usually emerge side by side [48].

IV. SUMMARY AND CONCLUSION

We performed hard x-ray holographic imaging with single XFEL pulses to investigate optical breakdown and cavitation following a focused femtosecond infrared laser pulse in water. Shapes and densities of laser-induced cavities were imaged with submicron resolution, and with a unique density-based quantitative contrast mechanism. For cavitation events of quasicylindrical symmetry, the emission of a weak shock wave was observed in the radial direction. The constant propagation speed which is reached after a few nanoseconds is consistent with the pressure inferred from the independently reconstructed shock wave. At the same time, we could observe the temporal density evolution in the cavity, consistent with mass conservation, as the plasma gradually evolves into a cavitation bubble.

The collective expansion of cavitation bubbles originating from multiple breakdown regions was also reconstructed and analyzed. Due to the deposited pulse energy being distributed over several plasma hot spots, the expansion of the main filament was found to be slower. Bubble fusion was observed only after approximately 500 ns, when separating thin water layers were disrupted. At lower laser pulse energy and in the center of the approximately 150 μm long breakdown region, multifilamentation led to the formation of multiple filament-like cavities with sub\micro m diameter and few μm spacing. This observation is consistent with theory for spacing of multiple filaments in collimated beams due to modulational instability. In summary, our measurements allow, for the first time, to observe the submicron structure and dynamics of filamentation and optical breakdown within a high-NA laser focus. By imaging the cavities, also in multibreakdown and multifilamentation regimes, we obtain a footprint of the complex intensity distribution within the focal volume which can form after nonlinear optical interaction of the laser pulse in water.

The experimental approach described in this work is fully capable of covering a more complete parameter space of pulse energy, focusing geometry, pulse duration or the role of aberrations, in the future. Especially systematic measurements at different positions along the optical axis can provide valuable insights into the formation and dynamics of (multi) filamentation during ultrafast pulse propagation within the focal volume. In this context, the investigation of the forward emitted supercontinuum spectrum and complementary knife-edge measurements of the focus or filament size are possible. In addition, extended simulations of the plasma formation, the transition to an elliptical cavitation bubble and the investigation of multiple laser-induced cavitation events and bubble interaction would be highly interesting [85].

Future development of seeded XFEL operation is promising in view of improved imaging conditions regarding stability and monochromaticity [86]. In fact, the resolution-limiting factor in the present experiment was due to chromatic aberration of the CRL optics. Imaging at lower photon energy, for example, at 14 keV, would improve the phase contrast and would probably also enable single-pulse resolution of shock wave emission from multiple breakdown spots. Finally, single-pulse x-ray imaging at XFELs can be extended to investigate fast hydrodynamics or laser-induced phenomena in strongly scattering and opaque materials and complex fluids such as blood and tissue, under conditions close to those used in femtosecond surgery.

ACKNOWLEDGMENTS

We thank P. Luley for engineering and preparation for the experimental setup. We further thank Bruno Fernandes (European XFEL, EEE, Fast Electronics) for his support. We acknowledge European XFEL in Schenefeld, Germany, for the provision of x-ray free-electron laser beamtime at MID and would like to thank the staff for their assistance. We acknowledge German Ministry for Research (BMBF) as a principal fund for this work through Project No. 05K22MG2 "ULFAHOL: Weiterentwicklung der Vollfeldbildgebungsmethode durch inline-Holographie am Instrument MID des European XFEL". Further, we acknowledge SFB 1456/C03 for additional support. M.V. and T.S. are members of the Max-Planck School of Photonics. This research was supported, in part, through the Maxwell computational resources operated at DESY. We acknowledge funding of the nanofocusing setup at MID through German Ministry for Research (BMBF) Project No. 05K13OD2 "Erzeugung und Charakterisierung von nanofokussierten XFEL-Pulsen zur Abbildung ultraschneller Prozesse in Materie". Finally, we thank VKT GmbH for providing the high-speed camera and the Kistler Group for providing the flash LED during the experiment.

The experiment was prepared by H. Hoeppe, with support from M. Vassholz, M. Osterhoff, and T. Salditt. During the beam time, the experiment was conducted by H. Hoeppe, M. Vassholz, J.M. Rosselló, M. Osterhoff, J. Hagemann, and T. Salditt, together with the MID team and supported by T. Engler. The data were analyzed by H. Hoeppe, with support from M. Osterhoff, J. Hagemann, J. M. Rosselló, and T. Salditt. The flat-field correction of the data was computed by J. Hagemann and T. Engler. The paper was mainly written by H. Hoeppe and T. Salditt, with review and editing support from all coauthors. This work was conceptualied by H. Hoeppe, J.M. Rosselló, M. Vassholz, J. Hagemann, M. Osterhoff, R. Mettin, and T. Salditt and administered by T. Salditt. The proposal for the XFEL beam time was written by H. Hoeppe and T. Salditt with support from M. Vassholz, J. Hagemann, M. Osterhoff, J.M. Rosselló, R. Mettin, A. Schropp, F. Seiboth, and C.G. Schroer.

DATA AVAILABILITY

The data that are used in this work are available from the authors upon reasonable request. Data recorded for the experiment at the European XFEL are available at [87].

[1] C. A. Sacchi, Laser-induced electric breakdown in water, J. Opt. Soc. Am. B **8**, 337 (1991).

[2] J. Noack and A. Vogel, Laser-induced plasma formation in water at nanosecond to femtosecond time scales: Calculation of thresholds, absorption coefficients, and energy density, IEEE J. Quantum Electron. **35**, 1156 (1999).

[3] P. Gibbon, *Short Pulse Laser Interactions With Matter: An Introduction* (World Scientific, Singapore, 2005).

[4] A. Vogel, J. Noack, G. Hüttman, and G. Paltauf, Mechanisms of femtosecond laser nanosurgery of cells and tissues, Appl. Phys. B **81**, 1015 (2005).

[5] N. Linz, S. Freidank, X.-X. Liang, and A. Vogel, Wavelength dependence of femtosecond laser-induced breakdown in water and implications for laser surgery, Phys. Rev. B **94**, 024113 (2016).

[6] D. X. Hammer, R. J. Thomas, M. Frenz, E. D. Jansen, G. D. Noojin, S. J. Diggs, J. Noack, A. Vogel, and B. A. Rockwell, Shock wave and cavitation bubble measurements of ultrashort-pulse laser-induced breakdown in water, in *Laser-Tissue Interaction VII*, Vol. 2681 (SPIE, Bellingham, WA, 1996), pp. 437–448.

[7] A. Vogel, S. Busch, and U. Parlitz, Shock wave emission and cavitation bubble generation by picosecond and nanosecond optical breakdown in water, J. Acoust. Soc. Am. **100**, 148 (1996).

[8] C. B. Schaffer, N. Nishimura, E. N. Glezer, A. M.-T. Kim, and E. Mazur, Dynamics of femtosecond laser-induced breakdown in water from femtoseconds to microseconds, Opt. Express **10**, 196 (2002).

[9] W. Lauterborn and A. Vogel, Shock wave emission by laser generated bubbles, in *Bubble Dynamics and Shock Waves*, edited by C. F. Delale (Springer, Berlin, 2013), pp. 67–103.

[10] V. Jukna, A. Jarnac, C. Milián, Y. Brelet, J. Carbonnel, Y.-B. André, R. Guillermin, J.-P. Sessarego, D. Fattaccioli, A. Mysyrowicz, A. Couairon, and A. Houard, Underwater acoustic wave generation by filamentation of terawatt ultrashort laser pulses, Phys. Rev. E **93**, 063106 (2016).

[11] V. Jukna, S. Albert, C. Millon, B. Mahieu, R. Guillermin, G. Rabau, D. Fattaccioli, A. Mysyrowicz, A. Couairon, and A. Houard, Control of the acoustic waves generated by intense laser filamentation in water, Opt. Express **30**, 9103 (2022).

[12] I. Akhatov, N. Vakhitova, A. Topolnikov, K. Zakirov, B. Wolfrum, T. Kurz, O. Lindau, R. Mettin, and W. Lauterborn, Dynamics of laser-induced cavitation bubbles, Exp. Therm Fluid Sci. **26**, 731 (2002).

[13] F. V. Potemkin and E. I. Mareev, Dynamics of multiple bubbles, excited by a femtosecond filament in water, Laser Phys. Lett. **12**, 015405 (2015).

[14] C. E. Brennen, *Cavitation and Bubble Dynamics* (Cambridge University Press, Cambridge, England, 2014).

[15] M. K. Bhuyan, A. Soleilhac, M. Somayaji, T. E. Itina, R. Antoine, and R. Stoian, High fidelity visualization of multiscale dynamics of laser-induced bubbles in liquids containing gold nanoparticles, Sci. Rep. **8**, 9665 (2018).

[16] A. Vogel and V. Venugopalan, Mechanisms of pulsed laser ablation of biological tissues, Chem. Rev. **103**, 577 (2003).

[17] A. Vogel, J. Noack, G. Hüttmann, and G. Paltauf, Mechanisms of femtosecond laser nanoprocessing of biological cells and tissues, J. Phys.: Conf. Ser. **59**, 249 (2007).

[18] T. Asshauer, C. Latz, A. Mirshahi, and C. Rathjen, Femtosecond lasers for eye surgery applications: Historical overview and modern low pulse energy concepts, Adv. Opt. Technol. **10**, 393 (2021).

[19] M. Calvarese, T. Meyer-Zedler, M. Schmitt, O. Guntinas-Lichius, and J. Popp, Recent developments and advances of femtosecond laser ablation: Towards image-guided microsurgery probes, TrAC Trends in Analytical Chemistry **167**, 117250 (2023).

[20] J. Marburger, Self-focusing: Theory, Prog. Quantum Electron. **4**, 35 (1975).

[21] W. Liu, O. Kosareva, I. Golubtsov, A. Iwasaki, A. Becker, V. Kandidov, and S. Chin, Femtosecond laser pulse filamentation versus optical breakdown in H2O, Appl. Phys. B **76**, 215 (2003).

[22] A. Couairon and A. Mysyrowicz, Femtosecond filamentation in transparent media, Phys. Rep. **441**, 47 (2007).

[23] L. Bergé, S. Skupin, R. Nuter, J. Kasparian, and J.-P. Wolf, Ultrashort filaments of light in weakly ionized, optically transparent media, Rep. Prog. Phys. **70**, 1633 (2007).

[24] *Self-Focusing: Past and Present: Fundamentals and Prospects*, Topics in Applied Physics, Vol. 114, edited by R. W. Boyd, S. G. Lukishova, Y. Shen, and C. Ascheron (Springer, New York, 2009).

[25] S. L. Chin, *Femtosecond Laser Filamentation*, Springer Series on Atomic, Optical, and Plasma Physics, Vol. 55 (Springer, New York, 2010).

[26] W. Liu, S. L. Chin, O. Kosareva, I. S. Golubtsov, and V. P. Kandidov, Multiple refocusing of a femtosecond laser pulse in a dispersive liquid (methanol), Opt. Commun. **225**, 193 (2003).

[27] F. V. Potemkin, E. I. Mareev, A. A. Podshivalov, and V. M. Gordienko, Laser control of filament-induced shock wave in water, Laser Phys. Lett. **11**, 106001 (2014).

[28] F. V. Potemkin, E. I. Mareev, A. A. Podshivalov, and V. M. Gordienko, Highly extended high density filaments in tight focusing geometry in water: From femtoseconds to microseconds, New J. Phys. **17**, 053010 (2015).

[29] C. B. Schaffer, A. Brodeur, J. F. García, and E. Mazur, Micromachining bulk glass by use of femtosecond laser pulses with nanojoule energy, Opt. Lett. **26**, 93 (2001).

[30] A. Ródenas, M. Gu, G. Corrielli, P. Paiè, S. John, A. K. Kar, and R. Osellame, Three-dimensional femtosecond laser nanolithography of crystals, Nat. Photonics **13**, 105 (2019).

[31] F. Zhang, Z. Nie, H. Huang, L. Ma, H. Tang, M. Hao, and J. Qiu, Self-assembled three-dimensional periodic micro-nano structures in bulk quartz crystal induced by femtosecond laser pulses, Opt. Express **27**, 6442 (2019).

[32] Z. Yan, J. Gao, M. Beresna, and J. Zhang, Near-field mediated 40 nm in-volume glass fabrication by femtosecond laser, Adv. Opt. Mater. **10**, 2101676 (2022).

[33] Y. Jia and F. Chen, Recent progress on femtosecond laser micro-/nano-fabrication of functional photonic structures in dielectric crystals: A brief review and perspective, APL Photonics **8**, 090901 (2023).

[34] T. Yan and L. Ji, Ultrafast laser filamentation in transparent solids, Ultrafast Science **3**, 0023 (2023).

[35] A. Brodeur and S. L. Chin, Band-gap dependence of the ultrafast white-light continuum, Phys. Rev. Lett. **80**, 4406 (1998).

[36] V. Kandidov, O. Kosareva, I. Golubtsov, W. Liu, A. Becker, N. Akozbek, C. Bowden, and S. Chin, Self-transformation of a powerful femtosecond laser pulse into a white-light laser pulse

in bulk optical media (or supercontinuum generation), Appl. Phys. B **77**, 149 (2003).

[37] L. He, Y. Li, Q. Zhang, and P. Lu, Ultra-broadband water window supercontinuum generation with high efficiency in a three-color laser field, Opt. Express **21**, 2683 (2013).

[38] J. A. Dharmadhikari, G. Steinmeyer, G. Gopakumar, D. Mathur, and A. K. Dharmadhikari, Femtosecond supercontinuum generation in water in the vicinity of absorption bands, Opt. Lett. **41**, 3475 (2016).

[39] C.-S. Brès, A. D. Torre, D. Grassani, V. Brasch, C. Grillet, and C. Monat, Supercontinuum in integrated photonics: Generation, applications, challenges, and perspectives, Nanophotonics **12**, 1199 (2023).

[40] H. L. Xu and S. L. Chin, Femtosecond laser filamentation for atmospheric sensing, Sensors **11**, 32 (2011).

[41] A. W. Miziolek, V. Palleschi, and I. Schechter, *Laser Induced Breakdown Spectroscopy* (Cambridge University Press, Cambridge, England, 2006).

[42] S. L. Chin and S. Lagacé, Generation of H_2, O_2, and H_2O_2 from water by the use of intense femtosecond laser pulses and the possibility of laser sterilization, Appl. Opt. **35**, 907 (1996).

[43] H. Kierzkowska-Pawlak, J. Tyczkowski, A. Jarota, and H. Abramczyk, Hydrogen production in liquid water by femtosecond laser-induced plasma, Applied Energy **247**, 24 (2019).

[44] A. Vogel, K. Nahen, D. Theisen, R. Birngruber, R. J. Thomas, and B. A. Rockwell, Influence of optical aberrations on laser-induced plasma formation in water and their consequences for intraocular photodisruption, Appl. Opt. **38**, 3636 (1999).

[45] D. V. Apeximov, O. A. Bukin, S. S. Golik, A. A. Zemlyanov, A. M. Kabanov, O. I. Kuchinskaya, A. Y. Mayor, G. G. Matvienko, V. K. Oshlakov, A. V. Petrov, E. B. Sokolova, and E. E. Khoroshaeva, Multiple filamentation of collimated Ti:Sapphire laser beams in water, Atmos. Oceanic Opt. **28**, 197 (2015).

[46] G. Méchain, A. Couairon, M. Franco, B. Prade, and A. Mysyrowicz, Organizing multiple femtosecond filaments in air, Phys. Rev. Lett. **93**, 035003 (2004).

[47] P.-P. Li, M.-Q. Cai, J.-Q. Lü, D. Wang, G.-G. Liu, S.-X. Qian, Y. Li, C. Tu, and H.-T. Wang, Control of femtosecond multi-filamentation in glass by designable patterned optical fields, AIP Adv. **6**, 125103 (2016).

[48] Y. E. Geints, S. S. Golik, A. A. Zemlyanov, A. M. Kabanov, and A. V. Petrov, Microstructure of the multiple-filamentation zone formed by femtosecond laser radiation in a solid dielectric, Quantum Electron. **46**, 133 (2016).

[49] Z. Wu, H. Jiang, L. Luo, H. Guo, H. Yang, and Q. Gong, Multiple foci and a long filament observed with focused femtosecond pulse propagation in fused silica, Opt. Lett. **27**, 448 (2002).

[50] D. Majus, V. Jukna, G. Tamošauskas, G. Valiulis, and A. Dubietis, Three-dimensional mapping of multiple filament arrays, Phys. Rev. A **81**, 043811 (2010).

[51] P. P. Kiran, S. Bagchi, S. R. Krishnan, C. L. Arnold, G. R. Kumar, and A. Couairon, Focal dynamics of multiple filaments: Microscopic imaging and reconstruction, Phys. Rev. A **82**, 013805 (2010).

[52] A. Couairon, L. Sudrie, M. Franco, B. Prade, and A. Mysyrowicz, Filamentation and damage in fused silica induced by tightly focused femtosecond laser pulses, Phys. Rev. B **71**, 125435 (2005).

[53] A. Schropp, R. Hoppe, V. Meier, J. Patommel, F. Seiboth, Y. Ping, D. G. Hicks, M. A. Beckwith, G. W. Collins, A. Higginbotham, J. S. Wark, H. J. Lee, B. Nagler, E. C. Galtier, B. Arnold, U. Zastrau, J. B. Hastings, and C. G. Schroer, Imaging shock waves in diamond with both high temporal and spatial resolution at an XFEL, Sci. Rep. **5**, 11089 (2015).

[54] D. S. Hodge, A. F. T. Leong, S. Pandolfi, K. Kurzer-Ogul, D. S. Montgomery, H. Aluie, C. Bolme, T. Carver, E. Cunningham, C. B. Curry, M. Dayton, F.-J. Decker, E. Galtier, P. Hart, D. Khaghani, H. J. Lee, K. Li, Y. Liu, K. Ramos, and J. Shang, Multi-frame, ultrafast, x-ray microscope for imaging shock-wave dynamics, Opt. Express **30**, 38405 (2022).

[55] P. Vagovič, T. Sato, L. Mikeš, G. Mills, R. Graceffa, F. Mattsson, P. Villanueva-Perez, A. Ershov, T. Faragó, J. Uličný, H. Kirkwood, R. Letrun, R. Mokso, M.-C. Zdora, M. P. Olbinado, A. Rack, T. Baumbach, J. Schulz, A. Meents, and H. N. Chapman, Megahertz x-ray microscopy at x-ray free-electron laser and synchrotron sources, Optica **6**, 1106 (2019).

[56] G. Rigon, B. Albertazzi, T. Pikuz, P. Mabey, V. Bouffetier, N. Ozaki, T. Vinci, F. Barbato, E. Falize, Y. Inubushi, N. Kamimura, K. Katagiri, S. Makarov, M. J.-E. Manuel, K. Miyanishi, S. Pikuz, O. Poujade, K. Sueda, T. Togashi, and Y. Umeda, Micron-scale phenomena observed in a turbulent laser-produced plasma, Nat. Commun. **12**, 2679 (2021).

[57] M. Vassholz, H. P. Hoeppe, J. Hagemann, J. M. Rosselló, M. Osterhoff, R. Mettin, J. Möller, M. Scholz, U. Boesenberg, J. Hallmann, C. Kim, A. Zozulya, W. Lu, R. Shayduk, A. Madsen, and T. Salditt, Structural dynamics of water in a supersonic shockwave, Phys. Fluids **35**, 016126 (2023).

[58] H. Soyama, X. Liang, W. Yashiro, K. Kajiwara, E. M. Asimakopoulou, V. Bellucci, S. Birnsteinova, G. Giovanetti, C. Kim, H. J. Kirkwood, J. C. P. Koliyadu, R. Letrun, Y. Zhang, J. Uličný, R. Bean, A. P. Mancuso, P. Villanueva-Perez, T. Sato, P. Vagovič, and D. Eakins, Revealing the origins of vortex cavitation in a Venturi tube by high speed X-ray imaging, Ultrasonics Sonochemistry **101**, 106715 (2023).

[59] K. Xiang, S. Huang, H. Song, V. Bazhenov, V. Bellucci, S. Birnsteinova, R. de Wijn, J. C. P. Koliyadu, F. H. M. Koua, A. Round, E. Round, A. Sarma, T. Sato, M. Sikorski, Y. Zhang, E. M. Asimakopoulou, P. Villanueva-Perez, K. Porfyrakis, I. Tzanakis, and D. G. Eskin, Ultrasound cavitation and exfoliation dynamics of 2d materials re-vealed in operando by x-ray free electron laser megahertz imaging, arXiv:2305.08538.

[60] J. M. Rosselló, H. P. Hoeppe, M. Koch, C. Lechner, M. Osterhoff, M. Vassholz, J. Hagemann, J. Möller, M. Scholz, U. Boesenberg, J. Hallmann, C. Kim, A. Zozulya, W. Lu, R. Shayduk, A. Madsen, T. Salditt, and R. Mettin, Jetting bubbles observed by x-ray holography at a free-electron laser: Internal structure and the effect of non-axisymmetric boundary conditions, Exp. Fluids **65**, 20 (2024).

[61] H. P. Hoeppe, M. Osterhoff, A. A. Maleki, J. M. Rosselló, M. Vassholz, J. Hagemann, T. Engler, D. Schwarz, A. Rodriguez-Fernandez, U. Boesenberg, J. Möller, R. Shayduk, J. Hallmann, A. Madsen, R. Mettin, and T. Salditt, The collapse of a sonoluminescent cavitation bubble imaged with X-ray free-electron laser pulses, New J. Phys. **26**, 033002 (2024).

[62] T. Salditt and A.-L. Robisch, Coherent x-ray imaging, in *Nanoscale Photonic Imaging*, edited by T. Salditt, A. Egner, and D. R. Luke (Springer International, Cham, Switzerland, 2020), pp. 35–70.

[63] J. Hagemann, M. Vassholz, H. Hoeppe, M. Osterhoff, J. M. Rosselló, R. Mettin, F. Seiboth, A. Schropp, J. Möller, J. Hallmann, C. Kim, M. Scholz, U. Boesenberg, R. Schaffer, A. Zozulya, W. Lu, R. Shayduk, A. Madsen, C. G. Schroer, and T. Salditt, Single-pulse phase-contrast imaging at free-electron lasers in the hard X-ray regime, J. Synchrotron Radiat. **28**, 52 (2021).

[64] M. Osterhoff, M. Vassholz, H. P. Hoeppe, J. M. Rosselló, R. Mettin, J. Hagemann, J. Möller, J. Hallmann, M. Scholz, R. Schaffer, U. Boesenberg, C. Kim, A. Zozulya, W. Lu, R. Shayduk, A. Madsen, and T. Salditt, Nanosecond timing and synchronization scheme for holographic pump–probe studies at the MID instrument at European XFEL, J. Synchrotron Radiat. **28**, 987 (2021).

[65] M. Vassholz, H. P. Hoeppe, J. Hagemann, J. M. Rosselló, M. Osterhoff, R. Mettin, T. Kurz, A. Schropp, F. Seiboth, C. G. Schroer, M. Scholz, J. Möller, J. Hallmann, U. Boesenberg, C. Kim, A. Zozulya, W. Lu, R. Shayduk, R. Schaffer, and A. Madsen, Pump-probe X-ray holographic imaging of laser-induced cavitation bubbles with femtosecond FEL pulses, Nat. Commun. **12**, 3468 (2021).

[66] A. Madsen, J. Hallmann, G. Ansaldi, T. Roth, W. Lu, C. Kim, U. Boesenberg, A. Zozulya, J. Möller, R. Shayduk, M. Scholz, A. Bartmann, A. Schmidt, I. Lobato, K. Sukharnikov, M. Reiser, K. Kazarian, and I. Petrov, Materials imaging and dynamics (mid) instrument at the european X-ray free-electron laser facility, J Synchrotron Rad **28**, 637 (2021).

[67] B. Lengeler, C. G. Schroer, M. Kuhlmann, B. Benner, T. F. Günzler, O. Kurapova, F. Zontone, A. Snigirev, and I. Snigireva, Refractive x-ray lenses, J. Phys. D **38**, A218 (2005).

[68] F. Seiboth, D. Brückner, M. Kahnt, M. Lyubomirskiy, F. Wittwer, D. Dzhigaev, T. Ullsperger, S. Nolte, F. Koch, C. David, J. Garrevoet, G. Falkenberg, and C. G. Schroer, Hard X-ray wavefront correction via refractive phase plates made by additive and subtractive fabrication techniques, J. Synchrotron Radiat. **27**, 1121 (2020).

[69] D. Paganin, *Coherent X-Ray Optics* (Oxford University Press, Oxford, 2006).

[70] See Supplemental Material at http://link.aps.org/supplemental/10.1103/c91c-zrm7 for an extended method section and additional graphics.

[71] P. Cloetens, W. Ludwig, J. Baruchel, D. Van Dyck, J. Van Landuyt, J. P. Guigay, and M. Schlenker, Holotomography: Quantitative phase tomography with micrometer resolution using hard synchrotron radiation x rays, Appl. Phys. Lett. **75**, 2912 (1999).

[72] E. Abraham, K. Minoshima, and H. Matsumoto, Femtosecond laser-induced breakdown in water: Time-resolved shadow imaging and two-color interferometric imaging, Opt. Commun. **176**, 441 (2000).

[73] L. F. Devia-Cruz, S. Camacho-López, R. Evans, D. García-Casillas, and S. Stepanov, Laser-induced cavitation phenomenon studied using three different optically-based approaches–An initial overview of results, Photon. Lasers Medicine **1**, 195 (2012).

[74] B. D. Strycker, M. M. Springer, A. J. Traverso, A. A. Kolomenskii, G. W. Kattawar, and A. V. Sokolov, Femtosecond-laser-induced shockwaves in water generated at an air-water interface, Opt. Express **21**, 23772 (2013).

[75] R. H. Cole, *Underwater Explosions* (Princeton University Press, Princeton, NJ, 1948).

[76] P. H. Rogers, Weak-shock solution for underwater explosive shock waves, J. Acoust. Soc. Am. **62**, 1412 (1977).

[77] M. J. Crocker, *Handbook of Acoustics* (John Wiley & Sons, New York, 1998).

[78] J. M. Rosselló and C.-D. Ohl, Bullet jet as a tool for soft matter piercing and needle-free liquid injection, Biomedical Optics Express **13**, 5202 (2022).

[79] A. B. Sieber, D. B. Preso, and M. Farhat, Cavitation bubble dynamics and microjet atomization near tissue-mimicking materials, Phys. Fluids **35**, 027101 (2023).

[80] Z. Zhang, S. Wei, P. Wang, W. Qiu, and G. Zhang, Progress in applications of laser induced cavitation on surface processing, Opt. Laser Technol. **170**, 110212 (2024).

[81] A. Takita and Y. Hayasaki, Dynamics of femtosecond laser-induced breakdowns in water, in *Laser Applications in Microelectronic and Optoelectronic Manufacturing VII*, Vol. 7201 (SPIE, Bellingham, WA, 2009), pp. 85–92.

[82] G. Fibich and A. L. Gaeta, Critical power for self-focusing in bulk media and in hollow waveguides, Opt. Lett. **25**, 335 (2000).

[83] Z. W. Wilkes, S. Varma, Y.-H. Chen, H. M. Milchberg, T. G. Jones, and A. Ting, Direct measurements of the nonlinear index of refraction of water at 815 and 407 nm using single-shot supercontinuum spectral interferometry, Appl. Phys. Lett. **94**, 211102 (2009).

[84] A. J. Campillo, S. L. Shapiro, and B. R. Suydam, Periodic breakup of optical beams due to self-focusing, Appl. Phys. Lett. **23**, 628 (1973).

[85] M. Koch, C. Lechner, F. Reuter, K. Köhler, R. Mettin, and W. Lauterborn, Numerical modeling of laser generated cavitation bubbles with the finite volume and volume of fluid method, using OpenFOAM, Computers & Fluids **126**, 71 (2016).

[86] S. Liu, C. Grech, M. Guetg, S. Karabekyan, V. Kocharyan, N. Kujala, C. Lechner, T. Long, N. Mirian, W. Qin, S. Serkez, S. Tomin, J. Yan, S. Abeghyan, J. Anton, V. Blank, U. Boesenberg, F. Brinker, Y. Chen, and W. Decking, Cascaded hard X-ray self-seeded free-electron laser at megahertz repetition rate, Nat. Photonics **17**, 984 (2023).

[87] T. Salditt, Cavitation dynamics studied by time-resolved high-resolution X-ray holography: Bubble nucleation and bubble collapse, DOI: https://doi.org/10.22003/XFEL.EU-DATA-002807-00 (2021).